

# Effects of Dynamics Behavior and Size Distribution of Supercooled Large Droplets on Ice Accretion Processes

ZHANG Dexin<sup>1</sup>, ZENG Tenghui<sup>2</sup>, WANG Liu<sup>1,2</sup>, SUN Bo<sup>1</sup>, CHENG Zikang<sup>1</sup>,  
FENG Jiaxin<sup>1</sup>, XIE Junlong<sup>1</sup>, CHEN Jianye<sup>1\*</sup>

1. School of Energy and Power Engineering, Huazhong University of Science and Technology, Wuhan 430074, P. R. China;

2. Wuhan Aviation Instrument Co., Ltd., Aviation Industry Corporation of China, Wuhan 430070, P. R. China

(Received 2 November 2024; revised 25 February 2025; accepted 15 March 2025)

**Abstract:** Accurate simulation of ice accretion of supercooled large droplet (SLD) is pivotal for the international airworthiness certification of large aircraft. Its complex dynamics behavior and broad particle size distributions pose significant challenges to reliable CFD predictions. A numerical model of multi-particle SLD coupling breaking, bouncing and splashing behaviors is established to explore the relationship between dynamics behavior and particle size. The results show that the peak value of droplet collection efficiency  $\beta$  decreases due to splashing. The bounce phenomenon will make the impact limit  $S_m$  of the water drops decrease. With the increase of the SLD particle size, the water drop bounce point gradually moves toward the trailing edge of the wing. The critical breaking diameter of SLD at an airflow velocity of 50 m/s is approximately 100  $\mu\text{m}$ . When the SLD particle size increases, the height of the water droplet shelter zone on the upper edge of the wing gradually decreases, and the velocity in the Y direction decreases first and then increases in the opposite direction, increasing the probability of SLD hitting the wing again. Large particle droplets have a higher effect on the impact limit  $S_m$  than smaller droplets. Therefore, in the numerical simulation of the SLD operating conditions, it is very important to ensure the proportion of large particle size water droplets.

**Key words:** supercooled large droplet (SLD); splash and bounce; break up effect; critical diameter; particle size distribution

**CLC number:** V211.3

**Document code:** A

**Article ID:** 1005-1120(2025)02-0201-11

## 0 Introduction

Under atmospheric icing conditions, the impingement of supercooled droplets on airfoil surfaces induces ice accretion, posing significant safety risks to aircraft operations<sup>[1-3]</sup>. A notable accident occurred on October 31, 1994, involving an ATR-72 turboprop aircraft that crashed under freezing rain conditions<sup>[4]</sup>. The U.S. National Transportation Safety Board (NTSB) investigation confirmed that the accident resulted from freezing precipitation exceeding the normal droplet icing environment defined in Federal Aviation Administration (FAA) air-

worthiness regulations Appendix C<sup>[5]</sup>. After two decades of meteorological research, the FAA formally introduced new airworthiness icing requirements (Amendment 140) in 2014, adding Appendix O<sup>[6]</sup> to address the hazards of supercooled large droplet (SLD) icing conditions. Compared to Appendix C conventional icing criteria, Appendix O specifies additional water droplet mass distribution parameters for SLD.

Research on SLD began in the 1970s. NASA pioneered experimental studies of large droplet icing in the icing research tunnel (IRT)<sup>[7-10]</sup>, successfully simulating SLD bimodal droplet spectra in 2005.

\*Corresponding author, E-mail address: jianye\_chen@hust.edu.cn.

**How to cite this article:** ZHANG Dexin, CENG Tenghui, WANG Liu, et al. Effects of dynamics behavior and size distribution of supercooled large droplets on ice accretion processes[J]. Transactions of Nanjing University of Aeronautics and Astronautics, 2025, 42(2):201-211.

<http://dx.doi.org/10.16356/j.1005-1120.2025.02.005>

However, limitations in spray systems restricted simultaneous generation of optimally matched large and small droplets due to fixed air pressure settings, resulting in deviations from Appendix O<sup>[6]</sup> target distributions. The Italian Aerospace Research Center CIRA icing wind tunnel<sup>[11]</sup> achieved freezing drizzle (FZDZ) conditions in Appendix O through multi-nozzle configurations and reduced nozzle pressure. AVIC Aerodynamics Research institute in China developed an icing tunnel capable of generating small (10—50  $\mu\text{m}$ ) and large (100—200  $\mu\text{m}$ ) droplet spectra with liquid water content (LWC) ranging 0.1—3.0  $\text{g}/\text{m}^3$  for component-level testing<sup>[12]</sup>. Although current domestic and international icing wind tunnels have acquired the capability to generate large water droplet clouds, the following technical challenges persist: The current icing wind tunnels are unable to fully meet the simulation requirements for SLD icing conditions. Specifically, icing wind tunnels still employ hot water for spraying, resulting in large-diameter water droplets failing to adequately meet supercooling requirements<sup>[13-14]</sup>. Additionally, horizontal spraying inevitably experiences gravitational settling of large droplets due to their weight<sup>[15]</sup>, which compromises test accuracy. Numerical simulation has emerged as an effective alternative to overcome experimental constraints.

Current SLD numerical studies primarily focus on droplet dynamics and size distribution characteristics. Liu et al.<sup>[16]</sup> numerically investigated SLD splashing and breakup effects on ice accretion, revealing that droplet fragmentation changed the trajectory and the impingement range, while reducing the water impact limit  $S_m$ . Splashing was found to decrease the peak value of droplet collection efficiency  $\beta$  while increasing the impact limits  $S_m$  of upper/lower surfaces by 6.14% and 3.71%, respectively. Mundo et al.<sup>[17]</sup> developed an empirical model for deposition/splashing processes using the critical threshold  $K_M$  to predict SLD splash rebound. Wright<sup>[18]</sup> proposed a conservative Eulerian framework incorporating splash/rebound mechanisms, extending the Mundo model with impact angle considerations. Honsek et al.<sup>[19]</sup> classified droplet-wall in-

teractions into splash, rebound, and breakup modes using the critical threshold  $K_M$  and Weber number  $We$ . Pilch et al.<sup>[20]</sup> established acceleration-induced breakup mechanisms, proposing critical based  $We$  criteria for droplet fragmentation. Zhang et al.<sup>[21]</sup> proposed a multifactor breakup criterion model to address limitations in SLD ice accretion simulations, grounded in enhanced mechanistic insights into droplet fragmentation. O'Rourke et al.<sup>[22]</sup> applied Taylor analogy breakup (TAB) models despite their limitations in multi-mode oscillation representation. Zhu et al.<sup>[23]</sup> investigated the effects of particle size distribution on water droplet impingement characteristics and ice accretion morphology, however, the studied particle size range (below 50  $\mu\text{m}$ ) fell outside the SLD criteria established in Appendix O. Li et al.<sup>[24]</sup> improved SLD trajectory predictions by incorporating droplet deformation and rebound effects, yet omitted breakup mechanisms. Kong et al.<sup>[25]</sup> demonstrated dominant large-droplet impacts on the droplet collection efficiency  $\beta$  but neglected the splashing phenomena.

Reference survey reveals that current research lacks consensus on the interaction between SLD impingement dynamics and size distribution, with limited research on comprehensively addressing the relationship between the two. This study employs FENSAP-ICE and FLUENT to numerically model SLD breakup, rebound, and splashing dynamics, analyzing droplet behavior-size dependencies through experimental validation. The findings provide the theoretical reference for SLD ice shape prediction and anti-de-icing system design.

## 1 Numerical Model

### 1.1 Mathematical equations

The Eulerian approach was employed to solve the air-water droplet two-phase flow, where both the air and water droplets are treated as continuous phases. The gas phase is governed by the conservation equations as

$$\frac{\partial \rho_a}{\partial t} + \frac{\partial(\rho_a u)}{\partial x} + \frac{\partial(\rho_a v)}{\partial y} + \frac{\partial(\rho_a w)}{\partial z} = 0 \quad (1)$$

$$\frac{\partial(\rho_a \mathbf{u}_a)}{\partial t} + \operatorname{div}(\rho_a \mathbf{u}_a^2) = \operatorname{div}(\mu \operatorname{grad} \mathbf{u}_a) - \nabla p + S_U \quad (2)$$

$$\frac{\partial(\rho_a T_s)}{\partial t} + \operatorname{div}(\rho_a \mathbf{u}_a T_s) = \operatorname{div}\left(\frac{\lambda}{C_{pp}} \operatorname{grad} T_s\right) + S_T \quad (3)$$

where  $T_s$ ,  $p$ ,  $\rho_a$ ,  $\mathbf{u}_a$  represent the temperature, the pressure, the air density, and the air velocity, respectively;  $u$ ,  $v$ ,  $w$  the velocity components in the  $x$ ,  $y$ ,  $z$  directions, respectively;  $\mu$  and  $\lambda$  the dynamic viscosity and the thermal conductivity of the fluid, respectively; and  $S_U$  and  $S_T$  the momentum source term and the energy source term, respectively.  $C_{pp}$  is the specific heat capacity at constant pressure.

To characterize the droplet impingement behavior, the concept of water droplet volume fraction is introduced. The continuity equation and the momentum equation for the droplet phase are solved, yielding the governing equations for droplet dynamics as

$$\frac{\partial \alpha}{\partial t} + \nabla \cdot (\alpha \mathbf{u}_d) = 0 \quad (4)$$

$$\frac{\partial(\alpha \mathbf{u}_d)}{\partial t} + \nabla \cdot (\alpha \mathbf{u}_d^2) = \frac{Re_d C_D}{24K} \alpha (\mathbf{u}_a - \mathbf{u}_d) + \alpha \left(1 - \frac{\rho_a}{\rho_d}\right) \frac{1}{Fr^2} \quad (5)$$

where  $\alpha$  represents the volume fraction of water droplets,  $\mathbf{u}_d$  the velocity vector of water droplets,  $\rho_d$  the density of water droplets,  $Re_d$  the Reynolds number of water droplets,  $C_D$  the drag coefficient,  $K$  the inertia parameter, and  $Fr$  the Froude number.

Reynolds number of water droplets yields

$$Re_d = \frac{\rho_a d \mathbf{u}_a \cdot (\mathbf{u}_a - \mathbf{u}_d)}{\mu} \quad (6)$$

where  $d$  denotes the diameter water droplets.

Inertia parameter  $K$  is

$$K = \frac{18\mu f}{\rho_d d^2} \quad (7)$$

The drag coefficient  $f$  is

$$f = \frac{Re_d C_D}{24} \quad (8)$$

Due to deformation of SLD during motion, the drag coefficient  $C_D$  in the momentum equation must be modified.

$$C_D = (1 - e)C_{D,\text{sphere}} + eC_{D,\text{disk}} \quad (9)$$

where  $e$  denotes the deformation factor, shown as

$$e = 1 - (1 + 0.007\sqrt{We})^{-6} \quad (10)$$

The ball resistance coefficient is

$$C_{D,\text{sphere}} = \begin{cases} \frac{24(1 + 0.15Re_d^{0.687})}{Re_d} & Re_d \leq 1000 \\ 0.44 & Re_d > 1000 \end{cases} \quad (11)$$

The disk resistance coefficient is

$$C_{D,\text{disk}} = \begin{cases} \frac{64(1 + 0.318Re_d^{0.792})}{\pi Re_d} & Re_d \leq 133 \\ 1.17 & Re_d > 133 \end{cases} \quad (12)$$

## 1.2 Water droplet breaking model

The dimensionless parameters governing droplet breakup into smaller droplets are  $We$  and  $Oh$ .  $We$  represents the ratio of inertial forces to surface tension forces, as

$$We = \frac{\rho_d \mathbf{u}_d^2 d}{\sigma_d} \quad (13)$$

where  $\sigma_d$  denotes the surface tension of water droplets.

$Oh$  relates viscous forces to inertial and surface tension forces<sup>[22]</sup>, shown as

$$Oh = \frac{\mu_d}{\sqrt{\rho_d \sigma_d d}} \quad (14)$$

where  $\mu_d$  is the droplet dynamic viscosity.

The governing equation describing the temporal evolution of droplet diameter mathematically characterizes the dynamic variation process of the diameter with time, shown as

$$\frac{Dd}{Dt} = -\frac{L - D_s}{\tau} \quad (15)$$

where  $L$  is the initial droplet diameter,  $D_s$  the stable droplet diameter, and  $\tau$  the relaxation time.

The total breakup time  $t$  depends on the breakup mechanism and local  $We$ , as defined by<sup>[26]</sup>

$$t = \begin{cases} 6(We - 12)^{-0.25} & 13 \leq We < 18 \\ 2.45(We - 12)^{0.25} & 18 \leq We < 45 \\ 14.1(We - 12)^{-0.25} & 45 \leq We < 351 \\ 0.766(We - 12)^{0.25} & 351 \leq We < 2670 \\ 5.5 & We \geq 2670 \end{cases} \quad (16)$$

When  $We < 13$ , droplet breakup does not occur, and the corresponding droplet diameter is the maximum stable droplet diameter  $d_{\text{stab}}$ , shown as

$$d_{\text{stab}} = \frac{12\sigma_d}{\rho_a \mathbf{u}_a \cdot (\mathbf{u}_a - \mathbf{u}_d)} \quad (17)$$

### 1.3 Splashing and bouncing model of water droplets

The splashing and bouncing phenomena occur during SLD impingement on airfoil surfaces are described by a semi-empirical model developed in Ref.[17]. This model determines the splash/bounce probability through the critical threshold  $K_M$ , as

$$K_M = K_C^{5/8} \quad (18)$$

where  $K_C$  represents the interplay between viscous, inertial and surface tension effects, shown as

$$K_C = WeOh^{-2/5} \quad (19)$$

Specifically, simultaneous splashing and bouncing occur when  $K_C \geq 540R^{-0.35}$ , where  $R$  is the equivalent sand-grain roughness height. Building on the Mundo's model, incorporated the effects of LWC and impact angle  $\theta$ , Wright<sup>[18]</sup> established the critical parameter  $K_w$  to determine the probability of splashing or bouncing, shown as

$$K_w = \frac{0.86K_Y}{(\sin \theta_i)^{5/4}} \left( \frac{LWC_i}{\rho_d} \right)^{-1/8} K_M^{1/2} \quad (20)$$

where  $\theta_i$  is the angle between the droplet velocity vector and the wall normal direction, and  $LWC_i$  the primary liquid water content.

Splashing occurs when  $K_w \geq 200$ . The relationship between the diameter ratio  $d_s/d_i$  of secondary droplets to primary droplets after splashing is governed by

$$\frac{d_s}{d_i} = 8.72e^{-0.028 \left( \frac{LWC_i}{\rho_d} \right)^{-1/8} K_M^2} \quad (21)$$

$$\frac{LWC_s}{LWC_i} = 0.7(1 - \sin \theta_i)(1 - e^{-0.0092026(K_w - 200)}) \quad (22)$$

$$\begin{cases} \frac{V_{ns}}{V_{ni}} = 0.03 - 0.02\theta_i \\ \frac{V_{ts}}{V_{ti}} = 1.075 - 0.0025\theta_i \end{cases} \quad (23)$$

where  $d_s$  and  $d_i$  denote the diameters of secondary droplets and primary droplets;  $LWC_s$  and  $LWC_i$  the liquid water contents of secondary droplets and primary droplets;  $V_{ns}$  and  $V_{ni}$  the normal velocities of secondary droplets and primary droplets; and  $V_{ts}$  and  $V_{ti}$  the tangential velocities of secondary droplets and primary droplets.

Bouncing occurs when  $K_w < 200$ , and the di-

ameter ratio of secondary droplets to primary droplets after bouncing is governed by

$$\frac{d_s}{d_i} = 1, \quad \frac{LWC_s}{LWC_i} = 1, \quad \frac{V_{ns}}{V_{ni}} = 1, \quad \frac{V_{ts}}{V_{ti}} = 1 \quad (24)$$

### 1.4 Terminal velocity

Tiny water droplets in the atmosphere remain stably suspended within cloud layers owing to their negligible gravitational settling velocity. However, once the droplet diameter exceeds a critical threshold, the droplets fail to remain suspended and instead develop a vertically downward velocity component (terminal velocity) under the influence of gravity.

Since the terminal velocity of droplets is inherently coupled with both  $C_D$  and  $Re_d$ , directly characterizing terminal velocity using  $Re_d$  alone presents significant challenges. To address this, Khan et al.<sup>[27]</sup> derived a functional relationship between  $Re_d$  and the Galileo number  $Ga$ , thereby enabling the determination of terminal velocity, as

$$u = \mu_d Re_d / \rho_d L = \mu_d [2.33Ga^{0.018} - 1.53Ga^{-0.016}]^{13.3} / \rho_d L \quad (25)$$

$$Ga = \frac{\rho_d^2 g L^3}{\mu_d^2} \quad (26)$$

where  $g$  is the gravitational acceleration.

## 2 Computational Modeling and Validation

### 2.1 Geometry and meshes

The computational model employs an NACA0012 airfoil with a characteristic length of 533 mm. Detailed structural parameters are illustrated in Fig.1.

The airfoil mesh was generated using Fluent Meshing. The far-field region employs tetrahedral

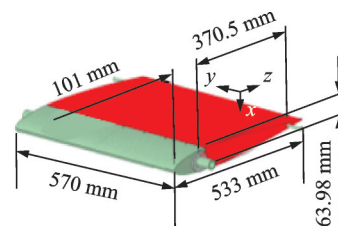


Fig.1 Wing model diagram

meshes. The boundary layer near the airfoil surface utilizes structured meshes, ensuring:

- (1) A near-wall  $y^+ < 1$  for the first grid layer.
- (2) A minimum of 10 boundary layer grids.
- (3) A boundary layer growth rate controlled within 1.2.

Detailed mesh characteristics are shown in Fig.2. To eliminate grid dependency effects, the grid independence study was conducted as follows: Maintained consistent mesh distribution patterns while varying the base mesh size to generate computational domains with  $1 \times 10^6$ ,  $2 \times 10^6$ ,  $3 \times 10^6$  and  $4 \times 10^6$  cells. Ensured the identical boundary conditions across all cases. Performed simulations and comparison results of pressure coefficient  $C_p$  are shown in Fig.3. The study revealed that the pressure coefficient remained nearly constant when the cell count exceeded  $2 \times 10^6$ . Consequently, the final simulation adopted the  $2 \times 10^6$  cells mesh for numerical computations.

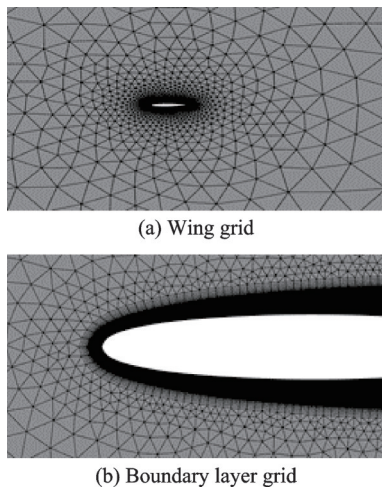


Fig.2 Wing mesh division

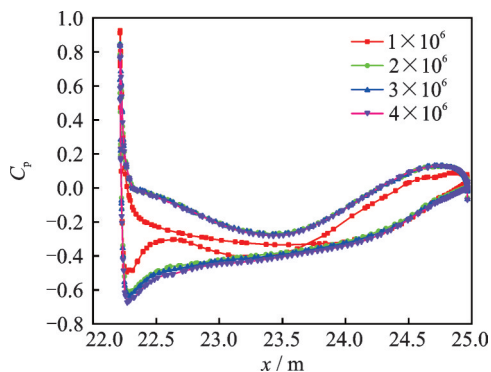


Fig.3 Distribution of pressure coefficient under different grid numbers

## 2.2 SLD model validation

To validate the accuracy of the SLD numerical model developed in this study, simulations were performed under experimental conditions replicating the AIWT wind tunnel. The boundary conditions are detailed in Table 1, and the experimental airfoil configuration corresponds to an NACA0012 profile with a chord length of 533 mm. In Table 1, AOA is the angle of attack, MVD is the median volume diameter of droplets, and FZDZ represents the frozen drizzle.

Table 1 Boundary conditions for icing cases

Number	Icing time/s	Velocity/ ( $\text{m}\cdot\text{s}^{-1}$ )	AOA/ ( $^\circ$ )	$T_s$ / $^\circ\text{C}$	LWC/ ( $\text{g}\cdot\text{m}^{-3}$ )	MVD/ $\mu\text{m}$
1	336	67	4	-19.2	1.04	160
2	660	95	0	-6.6	0.40	FZDZ
3	360	67	4	-19.4	1	20

A comparative analysis between the numerically simulated ice shapes and experimental ice shapes<sup>[25]</sup> was conducted, as shown in Fig.4. For single-droplet-size SLD cases, the simulated and experimental ice profiles exhibit similar overall contours, with minor discrepancies observed in localized surface fluctuations. Fig.5 illustrates the comparison for polydisperse SLD distributions. Notably, SLD ice accretion exhibits inherent stochasticity, manifested as variability in the number and position of ice horns. Despite this randomness, the simulated ice shapes align closely with experimental re-

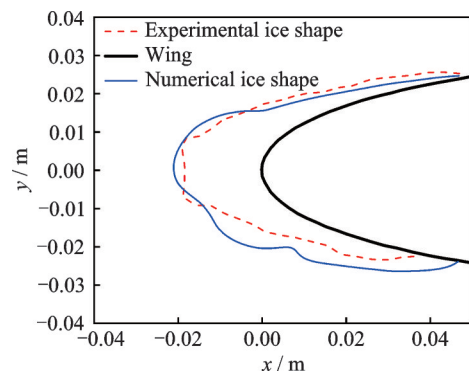


Fig.4 Comparison of ice shapes of SLD with single particle size

sults: Both display a depression at the airfoil stagnation point, leading to the formation of horn-shaped ice formations. For small-droplet icing cases (Fig.6), the experimental and simulated ice profiles demonstrate strong agreement, validating the model's robustness across droplet size regimes.

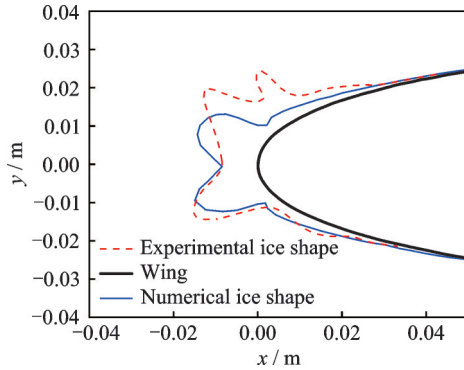


Fig.5 Comparison of ice shapes of SLD with multiple particle sizes

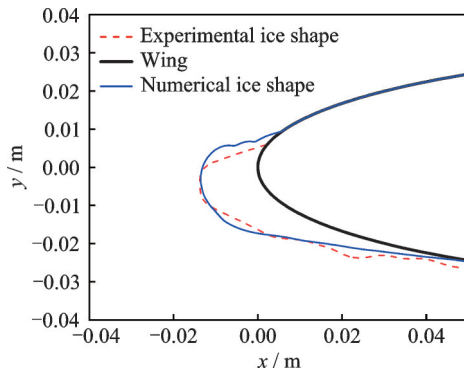


Fig.6 Comparison of small-droplet ice shapes

### 3 Results and Discussion

#### 3.1 Diameter effect on SLD splashing and bouncing dynamics

The dynamics behaviors of SLD, including rebound and breakup phenomena following airfoil impingement, were numerically investigated using the SLD splashing/bouncing model. Fig.7 compares the effects of SLD splashing and bouncing phenomena on the droplet collection efficiency  $\beta$  (with secondary droplet breakup-induced airfoil impingement excluded to accentuate bouncing characteristics). The splashing phenomenon reduces the peak value of  $\beta$ , while the bouncing behavior diminishes the impact limit  $S_m$ .

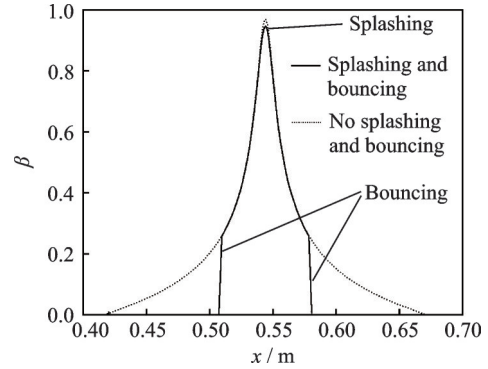


Fig.7 Effect of splashing and bouncing on droplet collection rate

Fig.8 presents the droplet collection efficiency  $\beta$  curves for SLDs with varying diameters under specified conditions of  $u_a = 95$  m/s,  $T_s = -6.6$  °C,  $LWC = 0.4$  g/m<sup>3</sup>. As the droplet diameter increases from 50  $\mu$ m to 100  $\mu$ m, the droplet collection efficiency  $\beta$  exhibits enhancement. This trend is attributed to increased droplet inertial forces associated with larger diameters, combined with compromised aerodynamic tracking capability, resulting in enhanced impingement tendencies on the airfoil surface. When the droplet diameter exceeds 100  $\mu$ m, the impact trajectories of differently sized droplets exhibit similarity with essentially stabilized  $\beta$ . Large diameter water droplets, subjected to enhanced inertial forces, demonstrate predominant splashing behavior upon impinging on the wing leading edge. As the impact location moves farther from the leading edge, droplets experience diminished normal forces, leading to increased bouncing tendencies. These two phase-change mechanisms are identified as the primary mechanisms responsible for run-

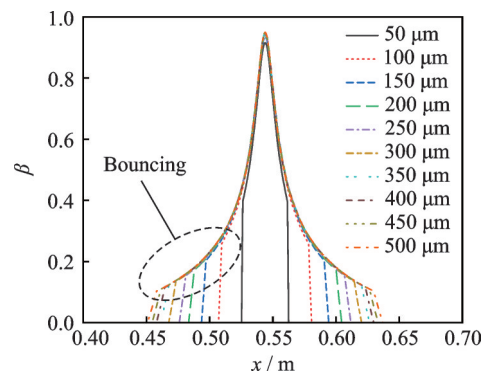


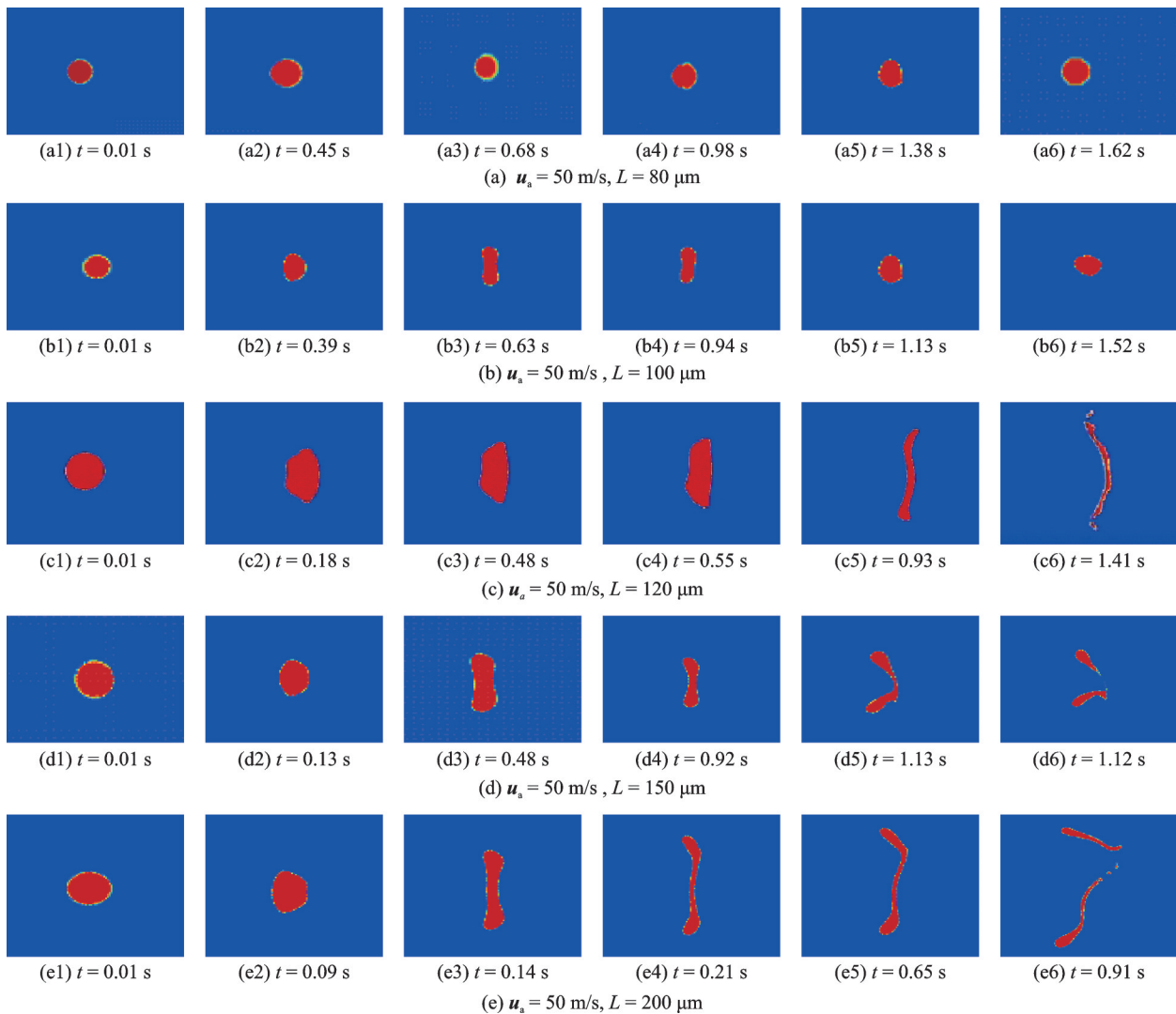
Fig.8 Collection rate curves of water droplets with different particle sizes

back ice accretion in supercooled large droplet conditions.

### 3.2 Diameter effect on SLD breakup dynamics

SLD experiences deformation with aerodynamic shear forces. When the shear stress exceeds the droplet's surface tension, breakup occurs, with the critical breakup diameter varying across flow velocities. Fig.9 compares the breakup behavior of SLDs with different initial diameters at airflow velocity of 50 m/s. As shown in Figs.9(a,b), water droplets with initial diameter of 80  $\mu\text{m}$  exhibits the negligible deformation under aerodynamic loading. When initial droplet diameters reach 100  $\mu\text{m}$ , aerodynamic loading induces oscillatory shape oscillations without breakup occurrence, with the  $We$  number ap-

proaching its critical threshold. Fig.9(c) illustrates the breakup process of water droplets with initial diameter of 120  $\mu\text{m}$  under aerodynamic loading, where windward-side deformation initiates, followed by progressive thinning of the liquid mass. Ultimately, aerodynamic compression leads to filamentous structural fragmentation. Figs.9(d,e) depict the breakup processes of water droplets with initial diameters of 150  $\mu\text{m}$  and 200  $\mu\text{m}$ . Both cases exhibit analogous deformation sequences under aerodynamic loading: (1) Initial windward surface curvature modification; (2) followed by progressive mid-section thinning with concavity formation; (3) culminating in aerodynamic shear stress-induced structural fragmentation through central ligament rupture.



Red: water droplets; Blue: air

Fig.9 Time evolution diagrams of water droplet fragmentation with different initial diameters

The critical breakup diameter is approximately 100  $\mu\text{m}$  at 50 m/s. According to the P&E breakup model<sup>[17]</sup>, increasing the airflow velocity will reduce the critical diameter.

Secondary droplets generated from SLD breakup under aerodynamic shear may undergo aerodynamic entrainment and subsequently re-impact the wing surface, altering the original LWC distribution and droplet velocity profiles.

Fig.10 compares the droplet collection efficiency  $\beta$  of the droplet with diameter of 500  $\mu\text{m}$  with and without secondary impact. The results demonstrate that secondary droplet impacts increase the droplet collection efficiency  $\beta$  near the airfoil leading edge, extending the ice accretion length.

Figs.11—13 present flow field comparisons for SLD with different initial diameters under specified conditions of  $u_a = 95 \text{ m/s}$  and  $\text{LWC} = 0.4 \text{ g/m}^3$ , considering the secondary impact. The results show that SLD exhibit marginal increments in  $x$ -compo-

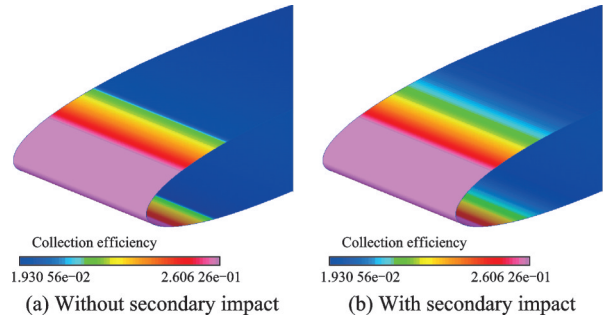


Fig.10 Comparison charts of droplet collection efficiency  $\beta$  under different SLD working conditions

nent velocity peaks with increasing droplet diameter, while  $y$ -component velocities demonstrate non-monotonic evolution initial reduction followed by directional reversal. Concurrently, the shadow zone height above the wing upper surface diminishes proportionally, attributed to gravitational dominance elevating terminal velocities. Larger SLDs post-breakup are more likely to impact unheated regions near the leading edge, forming runback ice, i.e., a critical hazard to flight safety compared to smaller droplets.

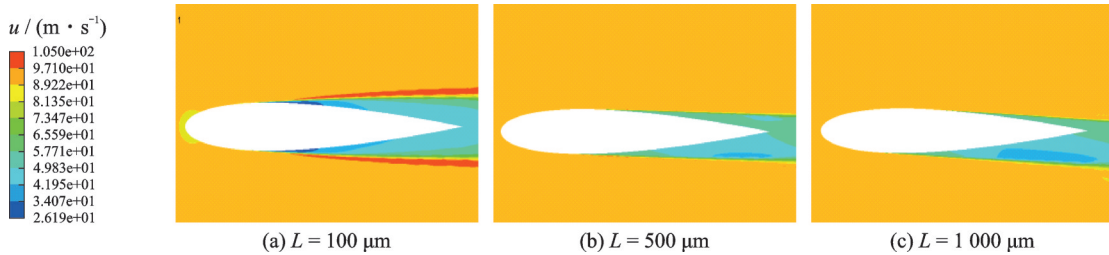


Fig.11 Comparison of  $x$ -direction velocities for different particle sizes

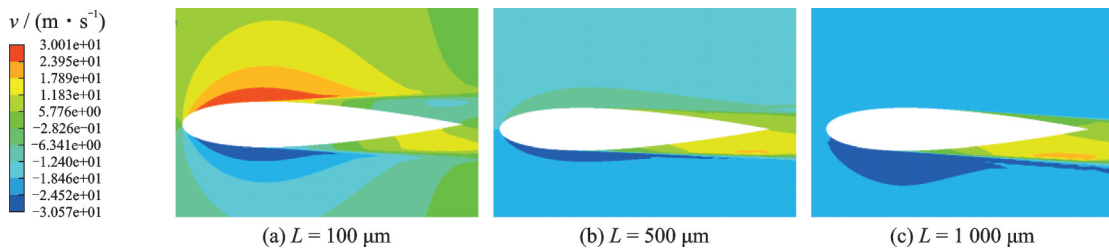


Fig.12 Comparison of  $y$ -direction velocities for different particle sizes

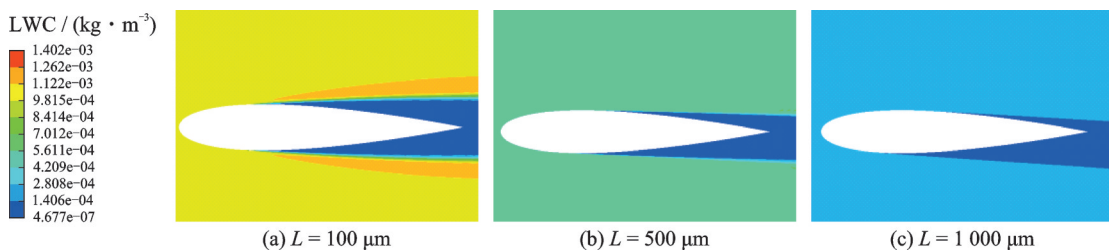


Fig.13 Comparison of LWC distribution with different particle sizes

### 3.3 SLD effect of particle size combination on $\beta$ and $S_m$

To investigate the effects of polydisperse droplet distributions on the droplet collection efficiency  $\beta$  and impact limit  $S_m$ , numerical simulations were conducted under icing wind tunnel conditions of  $u_a = 95$  m/s,  $T_s = -6.6$  °C,  $LWC = 0.4$  g/m<sup>3</sup>, integrating the previously developed breakup, bouncing, and splashing models.

Fig.14 compares the droplet collection efficiency  $\beta$  for small droplets with diameter of 20  $\mu\text{m}$ , large droplets with diameter of 100  $\mu\text{m}$ , and two polydisperse mixtures. As shown in Fig.14(a), adding 20% (in volume) water droplets with diameter of 100  $\mu\text{m}$  to the water droplets with diameter of 20  $\mu\text{m}$ , the peak value of droplet collection efficiency  $\beta$  increases, but the increase is not significant, while the impact limit  $S_m$  increases significantly. When adding 20% (in volume) water droplets with diameter of 20  $\mu\text{m}$  to the water droplets with diameter of 100  $\mu\text{m}$ , the impact limit  $S_m$  remains basically unchanged, while the peak value of droplet collec-

tion efficiency  $\beta$  slightly decreases. These findings indicate that large droplets exert comparable influence on the droplet collection efficiency  $\beta$  but dominate the impact limit  $S_m$  modulation compared to small droplets.

Fig.15 depicts ice shapes after 360 s for both polydisperse cases. While the spanwise ice coverage is similar, configurations with the higher large-droplet fractions exhibit the greater ice thickness at the leading edge. Horn-shaped ice formations at the stagnation point. Since  $\beta$  and  $S_m$  critically govern ice morphology, maintaining accurate large-droplet proportion in SLD simulations is essential for fidelity.

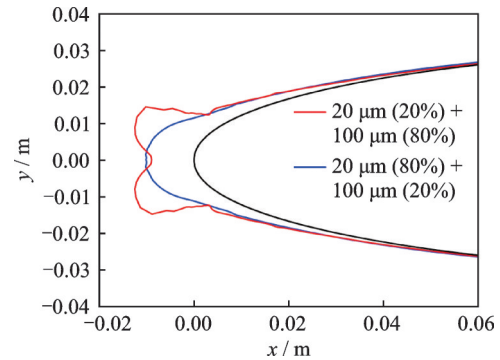


Fig.15 Comparison of ice shape for different particle size ratios (360 s ice accumulation time)

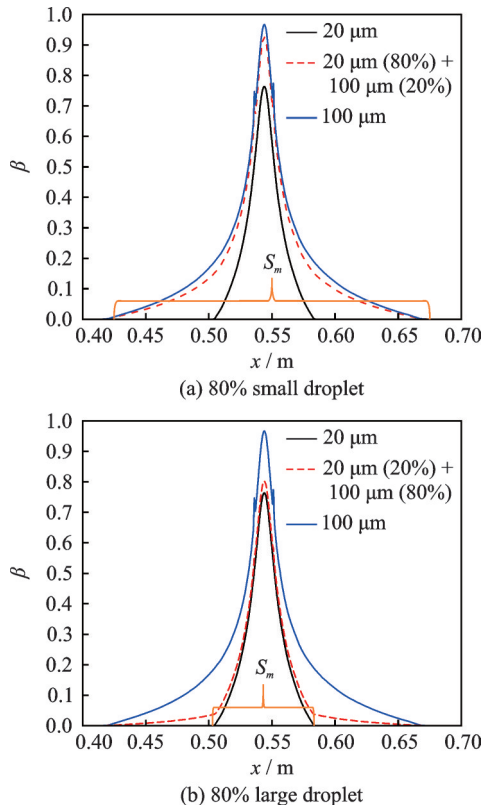


Fig.14 Comparison of droplets collection rates with different particle size ratios

## 4 Conclusions

To accurately simulate the SLD ice accretion, this paper developed a multi-droplet-size SLD impingement model that couples breakup, bouncing, and splashing behaviors, and validated it based on the experimental ice shapes in the AIWT wind tunnel. The key conclusions are as follows:

(1) During SLD impact on airfoil surfaces: Splashing reduces the droplet collection efficiency  $\beta$ . Bouncing decreases the impact limit  $S_m$ , with the bouncing onset point shifting rearward as droplet size increases, elevating ice accretion risk on the airfoil trailing edge.

(2) At an airflow velocity of 50 m/s, the critical breakup diameter is approximately 100  $\mu\text{m}$ . As diameter increases, the shadow zone height on the upper airfoil diminishes. The  $x$ -direction velocity gradually rises (marginally), while  $y$ -direction velocity initially decreases before reversing to in-

crease, enhancing droplet impingement likelihood on the trailing edge.

(3) Large droplets exert a significantly greater influence on the impact limit  $S_m$  compared to small droplets. Ensuring proportional inclusion of large droplets in SLD simulations is critical for achieving precise ice shape predictions.

## References

- [1] BRAGG M B. Experimental aerodynamic characteristics of an NACA 0012 airfoil with simulated glaze ice[J]. *Journal of Aircraft*, 1988, 25(9): 849-854.
- [2] POTAPCZUK M G, REINMANN J. Icing simulation: A survey of computer models and experimental facilities[C]//*Proceedings of the Fluid Dynamics Panel Specialists Meeting*. Cleveland Ohio: American Institute of Aeronautics and Astronautics, 1999.
- [3] COLE J, SAND W. Statistical study of aircraft icing accidents[C]//*Proceedings of the 29th Aerospace Sciences Meeting*. Boulder Colorado: National Center for Atmospheric Research, 1991.
- [4] BRAGG M, PERKINS W, SARTER N, et al. An interdisciplinary approach to inflight aircraft icing safety[C]//*Proceedings of the 36th AIAA Aerospace Sciences Meeting and Exhibit*. Reno, NV, USA: American Institute of Aeronautics and Astronautics, 1998.
- [5] Department of Transportation, FAA. Atmospheric icing conditions: 14 CFR Appendix C to Part 25[S]. [S.l.]: FAA, 2014.
- [6] Department of Transportation, FAA. Supercooled large droplet icing conditions: 14 CFR Appendix O to Part 25[S]. [S.l.]: FAA, 2014.
- [7] BRAGG M, BASAR T, PERKINS W, et al. Smart Icing Systems: Year 1 interim report[EB/OL]. (2014-07-19). <https://www.researchgate.net/publication/250323519>.
- [8] IDE R, OLDENBURG J. Icing cloud calibration of the NASA Glenn icing research tunnel[C]//*Proceedings of the 39th Aerospace Sciences Meeting and Exhibit*. Cleveland Ohio: American Institute of Aeronautics and Astronautics, 2001.
- [9] AL-KHALIL K, HITZIGRATH R, PHILIPPI O, et al. Icing analysis and test of a business jet engine inlet duct[C]//*Proceedings of the 38th Aerospace Sciences Meeting and Exhibit*. Reno, NV, USA: American Institute of Aeronautics and Astronautics, 2000.
- [10] STEEN L E, IDE R F, VAN ZANTE J F, et al. NASA Glenn icing research tunnel: 2014 and 2015 cloud calibration procedures and results: NASA/TM—2015-218758[R]. [S.l.]: NASA, 2015.
- [11] ESPOSITO B M, BROWN K J, BACHALO W D. Application of optical methods for icing wind tunnel cloud simulation extension to supercooled large droplets[C]//*Proceedings of the 23th Annual Conference on Liquid Atomization and Spray Systems*. Ventura, CA: American Institute of Aeronautics and Astronautics, 2011.
- [12] SHEN Hao, HAN Bingbing, LIU Zhenxia. Airworthiness certification of transport aircraft icing[M]. Shanghai: Shanghai Jiao Tong University Press, 2018. (in Chinese)
- [13] CAO Y, XIN M. Numerical simulation of supercooled large droplet icing phenomenon: A review[J]. *Archives of Computational Methods in Engineering*, 2020, 27(6): 1231-1265.
- [14] GUO Xiangdong, LIU Qinglin, LIU Senyun, et al. Numerical study of supercooled large droplet cloud evolution characteristics in icing wind tunnel[J]. *Acta et Astronautica Sinica*, 2020, 41(8): 123-155. (in Chinese)
- [15] ROCCO E T, HAN Y Q, KREEGER R, et al. Supercooled large droplet experimental reproduction, ice shape modeling, and scaling method assessment[J]. *AIAA Journal*, 2021, 59(4): 1277-1295.
- [16] LIU Feiyu, DENG Tian. Analysis of the influence of subcooled large water droplet dynamics on airfoil icing[J]. *Journal of Beijing University of Aeronautics and Astronautics*, 2024, 50(1): 173-186. (in Chinese)
- [17] MUNDO C H R, SOMMERFELD M, TROPEA C. Droplet-wall collisions: Experimental studies of the deformation and breakup process[J]. *International Journal of Multiphase Flow*, 1995, 21(2): 151-173.
- [18] WRIGHT W B. Further refinement of the LEWICE SLD model[C]//*Proceedings of the 44th AIAA Aerospace Sciences Meeting and Exhibit*. Reno, Nevada: AIAA, 2006.
- [19] HONSEK R, HABASHI W G, AUBÉ M S. Eulerian modeling of in-flight icing due to supercooled large droplets[J]. *Journal of Aircraft*, 2008, 45(4): 1290-1296.
- [20] PILCH M, ERDMAN C A. Use of breakup time data and velocity history data to predict the maximum size of stable fragments for acceleration-induced breakup of a liquid drop[J]. *International Journal of Multiphase Flow*, 1987, 13(6): 741-757.
- [21] ZHANG Chen, KONG Weiliang, LIU Hong. Study on the simulated crushing model of large-size supercooled water droplets[J]. *Aerodynamics*, 2013, 31

- (2): 144-150.
- [22] O'ROURKE P J, AMSDEN A. The TAB method for numerical calculation of spray droplet breakup: SAE Paper 872089[R]. [S.I.]: SAE, 1987.
- [23] ZHU Chengxiang, SUN Zhiguo, FU Bin, et al. Effect of droplet multi-size distribution on droplet impact properties and ice growth[J]. Journal of Nanjing University of Aeronautics and Astronautics, 2010, 42(5): 620-624. (in Chinese)
- [24] LI Zhonghui, LI Shiming, LIU Lei, et al. Numerical simulation of the motion and impact properties of supercooled large water droplets[J]. Mechanical Manufacturing and Automation, 2024, 53(4): 140-145. (in Chinese)
- [25] KONG Weiliang, ZHONG Xinyu, HAN Han, et al. Numerical simulation study of the mechanism of ice shape affecting the bimodal distribution characteristics of supercooled large water droplets[J]. Pneumatic Research and Testing, 2025, 3(1): 24-35. (in Chinese)
- [26] Ansys Inc. Ansys FENSAP-ICE user's manual[M]. 19.2 Version. Canonsburg, PA, USA: Ansys Inc, 2019.
- [27] KHAN A R, RICHARDSON J F. The resistance to motion of a solid sphere in a fluid[J]. Chemical Engineering Communications, 1987, 62(1/2/3/4/5/6): 135-150.

**Acknowledgement** This work was supported in part by the National Natural Science Foundation of China (No.

52276009).

#### Authors

**The first author** Mr. ZHANG Dexin received his B.S. degree in marine engineering from School of Mechanical Engineering, Dalian Maritime University, Dalian, China, in 2022. He is now pursuing the M.S. degree in Huazhong University of Science and Technology. He has focused on numerical simulation.

**The corresponding author** Dr. CHEN Jianye received the Ph.D. degree in refrigeration and cryogenic engineering from Zhejiang University, Zhejiang, China, in 2016. He is currently an associate professor with Huazhong University of Science and Technology, Wuhan, China. His research interest includes aircraft icing/anti-icing technology and numerical simulation of flow and heat transfer in complex environment.

**Author contributions** Mr. ZHANG Dexin designed the study, compiled the models and wrote the manuscript. Mr. ZENG Tenghui and Mr. WANG Liu conducted the analysis and interpreted the results. Mr. SUN Bo, Mr. CHENG Zikang, and Mr. FENG Jiaxin contributed to data for the analysis. Dr. CHEN Jianye guided the research and designed the article structure. Prof. XIE Junlong contributed to the design and discussion of the study. All authors commented on the manuscript draft and approved the submission.

**Competing interests** The authors declare no competing interests.

(Production Editor: SUN Jing)

## 过冷大水滴动力学行为及粒径分布形式对积冰过程的影响研究

张德新<sup>1</sup>, 曾腾辉<sup>2</sup>, 王柳<sup>1,2</sup>, 孙博<sup>1</sup>, 程梓康<sup>1</sup>, 冯佳昕<sup>1</sup>,  
谢军龙<sup>1</sup>, 陈建业<sup>1</sup>

(1. 华中科技大学能源与动力工程学院, 武汉 430074, 中国; 2. 武汉航空仪表有限责任公司, 武汉 430070, 中国)

**摘要:** 过冷大水滴 (Supercooled large droplet, SLD) 积冰冰形的准确模拟是大飞机国际飞行适航取证的关键技术, 其复杂的动力学特征和广泛的粒径分布形式是其难以使用 CFD 软件准确模拟的关键原因。针对此, 文中建立了耦合破碎、弹跳和飞溅行为的多粒径 SLD 数值模型, 探究其动力学行为与粒径的关系。结果表明: 飞溅现象会使水滴收集率  $\beta$  峰值降低, 弹跳现象会使水滴撞击极限  $S_m$  减小。随着 SLD 粒径增大, 水滴弹跳点逐渐往机翼后缘移动。50 m/s 空气流速下 SLD 的临界破碎直径约为 100  $\mu\text{m}$ , SLD 粒径增大时, 机翼上缘水滴遮蔽区高度逐渐减小, Y 方向速度先减小后反向增大, 增加了 SLD 再次撞击机翼的概率。大粒径水滴对水滴撞击极限  $S_m$  的影响高于小粒径水滴, 因此在 SLD 工况数值模拟中, 保证大粒径水滴占比至关重要。

**关键词:** 过冷大水滴; 飞溅弹跳; 破碎效应; 临界直径; 粒径分布